

# FRACTURE PROBABILITY OF MEMS OPTICAL DEVICES FOR SPACE FLIGHT APPLICATIONS

Rainer K. Fettig<sup>a</sup>, Jonathan L. Kuhn<sup>b</sup>, S. Harvey Moseley<sup>b</sup>,  
Alexander S. Kuttyrev<sup>a</sup>, Jon Orloff<sup>c</sup>

<sup>a</sup>Raytheon ITSS, Greenbelt, MD 20771

<sup>b</sup>NASA/Goddard Space Flight Center, Greenbelt, MD 20771

<sup>c</sup>University of Maryland, College Park, MD 20742

## ABSTRACT

A bending fracture test specimen design is presented for thin elements used in optical devices for space flight applications. The specimen design is insensitive to load position, avoids end effect complications, and can be used to measure strength of membranes less than  $2\ \mu\text{m}$  thick. The theoretical equations predicting stress at failure are presented, and a detailed finite element model is developed to validate the equations for this application. An experimental procedure using a focused ion beam machine is outlined, and results from preliminary tests of  $1.9\ \mu\text{m}$  thick single crystal silicon are presented. These tests are placed in the context of a methodology for the design and evaluation of mission critical devices comprised of large arrays of cells.

## NOMENCLATURE

$t$	beam thickness
$w_n, L_n$	narrow beam width and length
$w_w$	wide beam width
$a, b, c, d$	point locations
$F$	applied force
$L_a, L_b$	force distances
$\theta_b, \theta_c$	beam rotations
$E, G$	elastic and shear moduli
$I$	area moment of inertia
$\alpha$	load position factor
$M_b$	bending moment at point b
$\sigma_{xx}^{eq}, \sigma_{xx}^{fe}, \sigma_{p1}^{fe}$	theoretical and numerical stresses

## 1 MOTIVATION

NASA/Goddard Space Flight Center develops Micro-electromechanical System (MEMS) optical components for cryogenic space applications. Many of the devices are etched from  $2.0\ \mu\text{m}$  thick single crystal silicon or  $0.5\ \mu\text{m}$  thick silicon

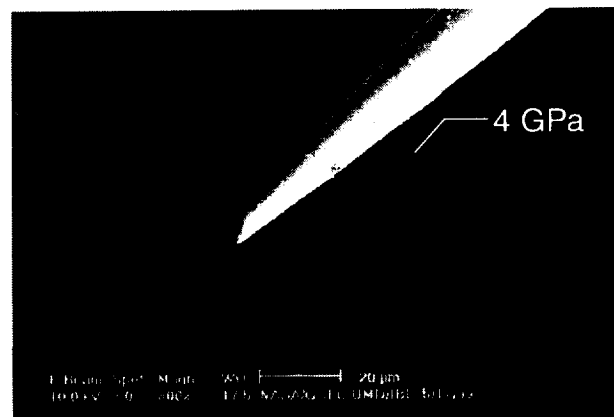


Figure 1: Micro-shutter element suspended from torsion bars, shown rotated almost  $180^\circ$ .

nitride membranes, involve extremely large deformations, and sustain huge permanent or periodic stresses during cooling and operation.

Examples of these applications are shown in Figs. 1 and 2. The first case is a large micro-shutter array patterned from  $0.5\ \mu\text{m}$  thick silicon nitride with a one side Aluminum layer of about  $20\ \text{nm}$ <sup>[1, 2]</sup>. The single shutter shown in Fig. 1 is comprised of a  $100\ \mu\text{m} \times 100\ \mu\text{m}$  blade suspended from a  $2.0\ \mu\text{m}$  wide torsion bar fixed at the ends. During operation the shutter is cooled to  $30\text{K}$  and repeatedly rotated  $90^\circ$ . The shutter is shown rotated almost  $180^\circ$  in the above figure, illustrating the flexibility of this material at these dimensions. Detailed finite element models based on bulk properties of silicon nitride predict a peak stress of  $4\ \text{GPa}$ , yet the bulk strength of hot pressed silicon nitride is on the order of  $800\ \text{MPa}$ .

The second example shown in Fig. 2 is an array of "pop-up"

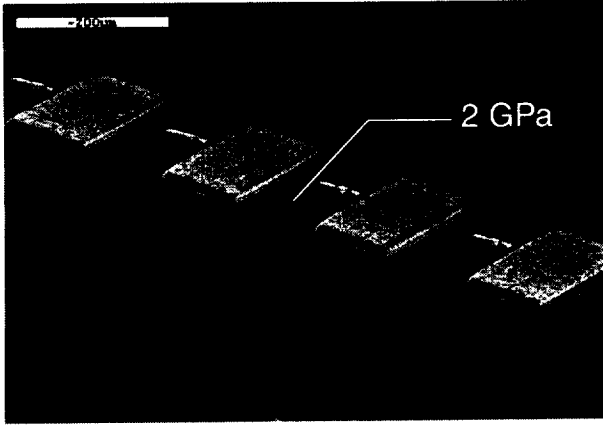


Figure 2: Pop-up Detectors shown in the permanent "folded" configuration.

detector elements<sup>[3]</sup>. The suspended pixel and support leg structures are initially etched from a flat single crystalline silicon membrane of  $2 \mu\text{m}$  nominal thickness. Each element contains an embedded bolometer. The central pixel area is coated with a  $10 \mu\text{m}$  thick layer of absorbing material such as bismuth. In the last fabrication step, the support legs are folded  $90^\circ$ , resulting in the free standing structures shown in Fig. 2. During operation the detectors are cooled to less than  $1\text{K}$ . A detailed finite element model predicts a peak stress of  $2 \text{ GPa}$  at the stress concentration due to the folding process, yet the bulk strength of single crystal silicon is  $200\text{-}300 \text{ MPa}$ .

Each of these device designs exploit the volume effect on strength of brittle materials. Initial design of the devices has been completed using trial and error, and qualitative simulations based on conservative estimates of stiffness and strength. Quantitative simulations based on accurate stiffness and statistical strength data are required to estimate the probability of device failure and to help guarantee device reliability during space flight. The mechanical material properties, in particular strength, vary with size and processing. As a result, inexpensive and convenient methods to measure properties of a large numbers of samples are needed.

In this paper we present the details of a dual width bending specimen used to measure the strength of thin membranes. Subsequently we discuss the application of this approach for the design and analysis of optical components etched from thin membranes.

## 2 DUAL WIDTH FRACTURE TEST

Simple cantilever beam test specimens suffer from the following limitations for thicknesses less than  $2 \mu\text{m}$ :

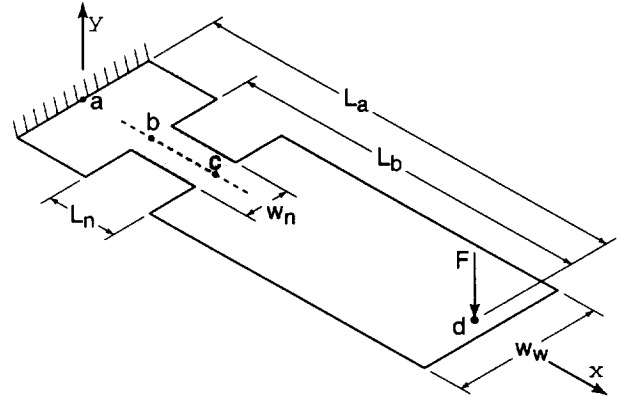


Figure 3: Dual width bending test specimen for brittle membranes less than  $2 \mu\text{m}$  thick.

1. Applied force is too small to measure directly.
2. Results strongly depend on force position.
3. Fixed end failure is complicated by end effects.
4. Very thin silicon and silicon nitride beams are too flexible and strong to break in bending at reasonable angles.

The dual width bending specimen of thickness  $t$  shown in Fig. 3 is designed to overcome these limitations. At the fixed end, the beam has a width  $w_w$ , which necks down to narrow width  $w_n$  for a length  $L_n$ . The remaining portion of the beam returns to width  $w_w$ . For a vertically applied load  $F$  at point  $d$  the peak stress will occur along the section at point  $b$  for  $w_w/w_n > L_a/L_b$ . Failure away from the fixed end avoids the complicated end effects mentioned in the third item above. In this configuration, the rotations at points  $b$  and  $c$ ,  $\theta_b$  and  $\theta_c$ , respectively, are measured just prior to failure using image processing. These rotations along with the elastic properties are used to compute the peak stress at point  $b$ , without knowing force  $F$ .

We also select  $w_w \gg w_n$  such that the wide portion of the beam shown in Fig. 3 is rigid relative to the neck region. This drives most deformation into the neck region, resulting in higher stresses at lower deflections, alleviating the last item above. This configuration also reduces the sensitivity to force location as shown in the following section.

### 2.1 Theoretical Equations

We may compute the relative rotation  $\theta_c - \theta_b$  of the neck region from beam theory, and use this to compute the peak stress at section  $b$ . For a vertical force  $F$  applied through the rigid wide beam at a distance  $L_b$  from point  $b$ , the relative rotation is

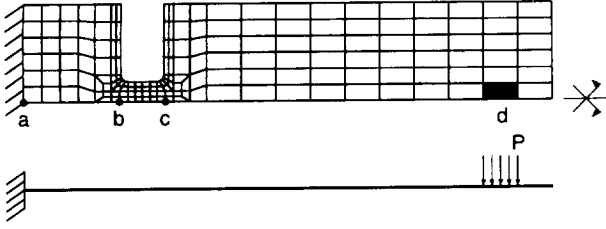


Figure 4: Detailed finite element model one symmetric half of the dual width fracture test specimen.

$$\theta_c - \theta_b = \frac{F(2L_b L_n - L_n^2)}{2EI} \quad (1)$$

where  $L_n$  is the length of the neck region,  $E$  is the Young's modulus, and  $I = w_n t^3/12$  is the cross section area moment of inertia of the neck region. For  $L_b = \alpha L_n$  the above equation can be rewritten as

$$\theta_c - \theta_b = \frac{F L_b L_n}{EI} \left(1 - \frac{1}{2\alpha}\right). \quad (2)$$

The resulting maximum moment  $M_b$  about point  $b$  is

$$M_b = F L_b = \frac{EI(\theta_c - \theta_b)}{L_n \left(1 - \frac{1}{2\alpha}\right)}. \quad (3)$$

The peak stress occurs at section  $b$  and is  $\sigma_{xx}^{eq} = M_b t/2I$ . Substituting equation (3) results in

$$\sigma_{xx}^{eq} = \frac{Et(\theta_c - \theta_b)}{2L_n \left(1 - \frac{1}{2\alpha}\right)} \quad (4)$$

The above equation is insensitive to force position for large  $\alpha = L_b/L_n$ . Even for smaller  $\alpha > 2$ , a small error in  $\alpha$  has little effect on the results. Consequently, only approximate measurement of the distance  $L_b$  is required to obtain reasonably accurate measures of stress. Small variations in force position during deformation will also have little effect on the results.

Equation (4) can be used to choose  $L_n$  such that the specimen will fail for small rotations. For the purpose of designing the specimen we consider a single crystal silicon membrane

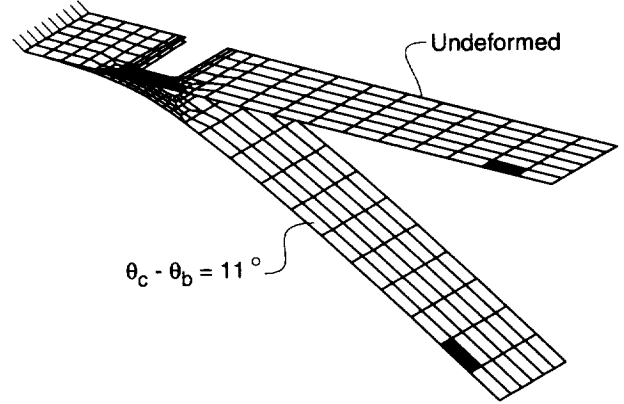


Figure 5: Deformations predicted by the finite element model.

and pick an arbitrary failure stress  $\sigma_f = 4 \text{ GPa}$ , which is double the average value of  $2 \text{ GPa}$  presented in Ref. 4. We align the length of the specimen with the  $\langle 110 \rangle$  direction and assume a modulus of  $E = 176 \text{ GPa}$ . For a thickness  $t = 1.9 \mu\text{m}$ , inclination  $\theta_c - \theta_b = 10^\circ$ , and scale factor  $\alpha = 10$ , equation (4) yields  $L_n = 7.5 \mu\text{m}$ . Therefore, a beam neck less than this length should result in failure at relatively small rotations. For convenience we chose  $L_n = 6.55 \mu\text{m}$  for the remaining studies in this paper.

The above equations are derived based on linear beam theory. A detailed plate finite element model is presented in the next section to validate the above equations for the dual width specimen configuration under large deflections, using the parameters specified above. Subsequently, test results are presented and used to compute the strength.

## 2.2 Finite Element Model

A detailed finite element model of the dual width specimen with parameters given above, widths  $w_n = 6.25 \mu\text{m}$  and  $w_w = 30 \mu\text{m}$ , and inside corner radius of  $1 \mu\text{m}$  is shown in Fig. 4. Only one symmetric half of the specimen geometry is modeled to reduce computation time and improve non-linear solution convergence. The finite element model is constructed of 166 four-node plate elements, and solutions were obtained using the non-linear geometry solution sequence in UAI/NASTRAN<sup>[5]</sup>.

For the orthotropic material properties, we use moduli  $E = 176 \text{ GPa}$  and  $G = 80 \text{ GPa}$  corresponding to the  $\langle 110 \rangle$  direction, moduli  $E = 130 \text{ GPa}$  and  $G = 50 \text{ GPa}$  corresponding to the  $\langle 100 \rangle$  direction, and Poisson's ratios of  $\nu = 0.279$  and  $\nu = 0.064$ , respectively. In this case the beam is located in the  $\{100\}$  plane aligned with the  $\langle 110 \rangle$  direction. All 6 degrees of freedom are fixed along the left edge and a normal

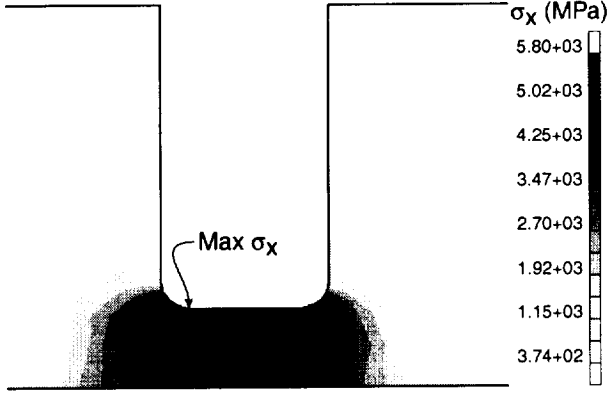


Figure 6: Bending test specimen used to measure strength.

pressure is applied to one element as shown in Fig. 4. This load is treated as a follower force such that the load remains normal to the element surface during deformation.

Deformation results predicted by the finite element model at a relative rotation of  $\theta_c - \theta_b = 11^\circ$  are shown at true scale in Fig. 5. The above figure illustrates that the end deflection is relatively large, and that slight rotation does occur at point  $b$  as expected. Stress contour fringes of the finite element stress predictions in the  $x$  direction  $\sigma_{xx}^{fe}$  are shown in the neck region in Fig. 6. As expected, the peak stress occurs in the neck region.

The maximum principal stress  $\sigma_{p1}^{fe}$  and  $x$  component of stress  $\sigma_{xx}^{fe}$  are listed in Table 1 for increasing relative rotation  $\theta_c - \theta_b$ . Corresponding values of  $\sigma_{xx}^{eq}$  computed from equation (4) are also listed and compared to the finite element predictions. The theoretical and finite element results are in excellent agreement for  $\sigma_{xx}$ . Brittle failure will most likely be driven by the maximum principal stress which is about 10% higher than the  $x$  component. As a result the theoretical equation will underpredict strength. This is acceptable and even desirable because it is conservative.

There is a concentration in stress due to the inside corner. The finite element method underpredicts the peak stresses due to averaging over each element. Equation (4) does not account for the stress concentration and as a result yields conservative estimates of strength. Hence there is good agreement through cancellation of errors. As a result the strength predictions presented herein are well suited for comparison with finite element results for actual structures such as the micro-shutters and pop-up detectors.

The above analysis validates equation (4) for predicting the strength using the dual width fracture test specimen. In the next section we use this equation to estimate the strength of single crystal silicon using the fracture test.

Load Step	$\theta_c - \theta_b$	Maximum Stress (GPa)			$\frac{\sigma_{xx}^{fe} - \sigma_{xx}^{eq}}{\sigma_{xx}^{fe}} \times 100\%$
		$\sigma_{p1}^{fe}$	$\sigma_{xx}^{fe}$	$\sigma_{xx}^{eq}$	
1	2.2	1.22	1.09	1.05	3.3
2	4.5	2.44	2.19	2.11	3.7
3	6.7	3.67	3.29	3.16	4.1
4	9.0	4.90	4.40	4.20	4.5
5	11.2	6.14	5.52	5.24	4.9
6	13.4	7.37	6.63	6.28	5.3
7	15.6	8.60	7.75	7.30	5.8
8	17.7	9.82	8.87	8.32	6.2
9	19.9	11.02	9.98	9.32	6.6
10	22.0	12.22	11.09	10.32	7.0

TABLE 1: Comparison of results for  $w_n = 6.25 \mu m$ ,  $L_n = 6.55 \mu m$ ,  $w_w = 30 \mu m$ ,  $L_a = 73.5 \mu m$ ,  $L_b = 58.5 \mu m$ ,  $\alpha = 8.9$ .

### 2.3 Experimental Measurements

All experiments were performed in an FEI 620 focused ion beam milling machine. The FEI 620 is a dual beam machine, with an ion and electron column, which allows ion milling and *in situ* scanning electron microscopy. Ion milling can be performed with ion beam spot sizes of 20 nm to 1  $\mu m$  and machining rates in silicon up to 10  $\mu m^3/s$ . The machine is also equipped with a micro-manipulator needle and the ability to deposit platinum by ion induced metal organic chemical vapor deposition (MOCVD).

The above platform was used to machine and test the dual width geometry from single crystal silicon membranes with the parameters specified in the previous section. The micro-manipulator is used to gradually apply the vertical load  $F$  to failure. A series of scanning electron microscope (SEM) images are recorded, and the last image prior to fracture is analyzed to extract the rotation angles  $\theta_c$  and  $\theta_b$ . These angles are used in conjunction with equation (4) to compute the peak stress.

Prior to bending, a light line is etched through the center of the neck region using the focused ion beam (shown as a dashed line in Fig. 3). A deformed cantilever specimen is shown in Fig. 7. The image just prior to failure is analyzed by drawing lines tangent to the etch line at points  $b$  and  $c$  as shown in Fig. 7. Horizontal and vertical reference lines are added. The base and height dimensions of the resulting triangles are measured and transformed to account for the image angle relative to the specimen plane. These dimensions are used to calculate the rotation angles.

Using the above procedure, the relative rotations were measured just prior to failure for 9 specimens, and the corresponding peak stress was calculated. The results are listed in Ta-

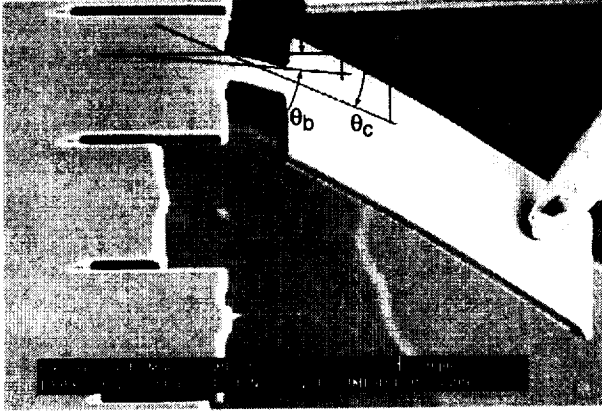


Figure 7: Scanning electron micrograph of a bending test specimen used to measure strength.

ble 2. The average stress at failure was found to be 14.2 GPa with a standard deviation of 1.37 GPa.

Wilson et. al. [4] presented strengths in the range of 1-2 GPa for micro-cantilever silicon beams with thickness of 30  $\mu m$ . However, in the study presented herein, the membrane thickness is 1.9  $\mu m$ , and the membranes are coated with metallic substances. These aspects will lead to strengths that are different from values presented elsewhere. The membranes are also so thin that simple cantilever beam tests tend to bend beyond 90° before failure, making it difficult to ascertain strength.

The above failure stress values are on the same order as those reported by Johansson et. al. [6], but much greater than the values presented by Wilson et. al. [4]. This is consistent with the fracture theory that smaller volume results in fewer flaws and higher strengths. Here we have thicknesses less than one tenth of the thicknesses used by Wilson et. al. [4]. The coating material may also provide a small increase of the strength [6].

Here we note that the results presented in Table 2 are highly approximate. In practice we found it difficult to accurately measure the rotation angles directly. As a result the rotations in Table 2 are only within  $\pm 5$  degrees, which represents an error of  $\pm 15$  to 20% for the angles listed in the table. The stresses computed using equation (4) are directly proportional to these angles, which means the listed stresses are within  $\pm 15$  to 20%. Ultimately, this method requires improved methods of determining the rotation angles to yield reliable results.

### 3 FRACTURE PROBABILITY METHODOLOGY

Traditionally researchers use the most accurate test methods available to measure and catalogue statistical brittle strength

Test	$L_n \mu m$	$\alpha = L_b/L_n$	$(\theta_c - \theta_b)^\circ$	$\sigma_{xx}^{eq} GPa$
15	6.4	4.8	26	13.4
16	6.6	6.8	34	16.5
17	6.5	6.0	32	15.9
18	6.4	6.2	29	14.6
19	6.4	5.2	28	14.4
20	6.4	5.2	26	13.4
21	6.1	4.1	26	14.4
22	6.3	5.9	24	12.4
25	6.5	3.4	24	12.9

TABLE 2: Fracture stresses computed from experimental measurements for  $t = 1.9 \mu m$ . The average is 14.2 GPa and the standard deviation is 1.37 GPa. The angles were measured with an accuracy of  $\pm 5$  degrees.

data in material libraries, handbooks, or archived literature. We typically use such cataloged data for the purposes of design of large scale brittle structures, perhaps complimented with some critical testing prior to fabrication. Once the structure is fabricated we inspect and test a prototype or production unit under environments that envelope anticipated service loads.

There are key drawbacks to this procedure for the development of MEMS devices that endure substantial stresses. Most importantly, strength is strongly a function of processing. In large scale structures processing effects are minimized by eliminating edges from the design and applying post fabrication surface treatments to reduce the population of surface flaws. MEMS edges left by etching can not be removed, and there are limited post etching treatments available. MEMS devices are also extremely sensitive to process variations across a wafer processed in batch. For example, the micro-shutter array described earlier will ultimately be comprised of at least 1024 by 1024 elements. At 100  $\mu m$  each this adds up to about 10 cm. As a result, for applications where reliable performance is critical the above traditional procedure is not adequate.

Development of such devices requires simple and convenient tests, even at the expense of some accuracy, as long as the results are conservative. Initially a large number of test samples may be fabricated and tested with the specific process anticipated for a given device. This data may be used to complete the design using Weibull statistical analysis as described in Ref. 7. Ultimately, a few witness samples could then be included at various locations in the actual device fabrication. Tests from these witness samples can then be compared with the larger data set to validate the resulting process and ultimately the actual strength of the fabricated device.

#### 4 CONCLUSION

In this work we presented a dual width fracture test specimen that helps alleviate several difficulties associated with simple cantilever tests. In particular, load position sensitivity is reduced and complications due to end effects are eliminated. This specimen geometry also allows the strength to be approximated without knowing loads which are difficult to resolve. This specimen may be used for membranes less than  $2\text{ }\mu\text{m}$  thick. Bending test methods are attractive because they provide relatively convenient witness samples.

While this specimen does reduce the force position sensitivity needed to accurately compute stress, the test does suffer from some of the same shortcomings of any bending test at these scales. In particular, the results are strongly dependent on accurate metrology, and are based on a presumed elastic modulus. There are also some concerns regarding the merits of bending tests compared to uniaxial tension tests<sup>[8]</sup>. Failure in bending is due to highly localized stresses, and does not account for the overall distribution of flaws in a volume, which may yield overly optimistic results. In this case, however, the bending test closely mimics actual load configurations in our devices.

The results presented here are promising for future investigations. In particular, each of our devices operate at cryogenic temperatures, and it will be important to understand the temperature effects on strength. These tests are also amenable to fatigue testing by placing an electrode near the specimen and cycling the applied voltage. These results are inherently less accurate than uniaxial tension tests which measure both force and deflection<sup>[9]</sup>. As a result, it will be important to rigorously validate these results with more accurate uniaxial tension tests.

#### ACKNOWLEDGEMENTS

The authors gratefully acknowledge Mary Li from Raytheon ITSS for providing the SEM image of the pop-up detectors.

#### REFERENCES

- [1] Moseley, S., Fettig, R., Kutyrev, A., Bowers, C., Kimble, R., Orloff, J. and Woodgate, B., *Programmable 2-Dimensional Microshutter Arrays*, *Micromachining and Microfabrication*, Vol. 3878, Sep. 1999.
- [2] Fettig, R., Kuhn, J., Moseley, S., Kutyrev, A., Orloff, J. and Lu, S., *Some Aspects on the Mechanical Analysis of Micro-shutters*, *Micromachining and Microfabrication*, Vol. 3875, Sep. 1999.
- [3] Li, M., Allen, C., Gordon, S., Kuhn, J., Mott, D., Stahle, C. and Wang, L., *Fabrication of Pop-up Detector Arrays on Si Wafers*, *Micromachining and Microfabrication*, Vol. 3874, Sep. 1999.
- [4] Wilson, C., Ormeggi, A. and Narbutovskih, M., *Fracture testing of silicon microcantilever beams*, *J. Appl. Phys.*, Vol. 79, No. 5, pp. 2386–2393, Mar. 1996.
- [5] Universal Analytics, Inc., Torrance, CA, UAI/NASTRAN User's Guide for Version 20.0, 1997.
- [6] Johansson, S., Ericson, F. and Schweitz, J.-A., *Influence of surface coatings on elasticity, residual stresses, and fracture properties of silicon microelements*, *J. Appl. Phys.*, Vol. 65, No. 1, pp. 122–128, Jan. 1989.
- [7] Greek, S., Ericson, F., Johansson, S. and Schweitz, J., *In situ tensile strength measurement and Weibull analysis of thick film and thin film micromachined polysilicon structures*, *Thin Solid Films*, Vol. 292, pp. 247–254, 1997.
- [8] Johnson, G., Jones, P. and Howe, R., *Materials Characterization for MEMS - A Comparison of Uniaxial and Bending Tests*, *Micromachining and Microfabrication*, Vol. 3874, Sep. 1999.
- [9] Sharpe, W., Yuan, B., Vaidyanathan, R. and Edwards, R., *Measurements of Young's Modulus, Poisson's Ratio, and Tensile Strength of Polysilicon*, *MEMS97*, pp. 424–429, 1997.